Available online at www.sciencedirect.com
SCIENCE DIRECT®
Earth and Planetary Science Letters 244 (2006) 170–185
EPSL
www.elsevier.com/locate/epsl

The role of prokaryotes in supergene alteration of submarine hydrothermal sulfides

S. Glynn [a,b], R.A. Mills [a,*], M.R. Palmer [a], R.D. Pancost [c], S. Severmann [d], A.J. Boyce [e]

[a] School of Ocean and Earth Science, National Oceanography Centre, Southampton, University of Southampton, Southampton SO14 3ZH, UK
[b] Hancock Museum, University of Newcastle, Newcastle, NE2 4PT, UK
[c] School of Chemistry, University of Bristol, Bristol BS8 1TS, UK
[d] Department of Earth Sciences, University of California Riverside, Riverside, CA 92521, USA
[e] Scottish Universities Environmental Research Centre, Rankine Ave., East Kilbride, Glasgow GW75 0QF, UK

Received 1 September 2005; received in revised form 17 January 2006; accepted 24 January 2006
Available online 15 March 2006
Editor: H. Elderfield

Abstract

We combine mineralogical, stable isotope and organic biomarker data to understand the role of prokaryote activity in supergene reactions within submarine hydrothermal sulfidic sediments. Data are presented for two adjacent cores from the periphery of the inactive *Alvin* hydrothermal mound. The limit of oxygenated seawater penetration into the sulfidic sediments is expressed as a sharp peak in solid phase Cu (atacamite and secondary Cu sulfides) associated with supergene alteration of the sulfide pile. Total prokaryote numbers are low throughout the upper few metres of sediment relative to published data for deep-sea sites. However, there is a statistically significant enrichment of prokaryote numbers at the redox front that coincides with abundant Fe-oxide filaments and a unique distribution of microbial biomarkers. The dominance of quaternary-branched alkanes in the oxidized transition zone immediately above the redox front (and their absence below) suggests a significant role of the source organisms in iron or sulfide oxidation under the more circumneutral conditions associated with the redox transition zone. The morphology of the Fe-oxide filaments preserved within late stage silica and gypsum mineralization is consistent with a biogenic origin of the filaments. Gypsum sulfur isotopes are in equilibrium with fluids that are derived from quantitative sulfide oxidation and gypsum nucleation is inferred to be biologically induced. These new data suggest that supergene alteration of sulfidic sediments generates sharp redox and pH gradients that stimulate prokaryotic activity, in particular iron and sulfide oxidisers, which in turn govern the distribution of secondary mineral phases and the abundance of redox sensitive trace metals.

Keywords: supergene alteration; biomineralisation; Fe oxidation

1. Introduction

Large numbers of prokaryote cells have been enumerated in a variety of sedimentary settings to depths of up to 800 m below the seafloor (e.g., [1]).

* Corresponding author. Tel.: +44 23 8069 2678; fax: +44 23 8059 3052.
E-mail address: ram1@noc.soton.ac.uk (R.A. Mills).

0012-821X/$ - see front matter © 2006 Elsevier B.V. All rights reserved.
doi:10.1016/j.epsl.2006.01.065

Approximately 10–30% of the cells are viable and metabolically active, even at several 100 m depth [2]. Some of the lowest cell counts observed in the upper few metres of deep-sea sediments come from metalliferous sediments associated with mid-ocean ridge hydrothermal systems [3] and eastern equatorial Pacific open ocean sites [4]. The low cell abundance, coupled to very low levels of reaction products in pore fluids, have been taken to imply low net metabolic reaction rates in these sediments [3,4]. Alternative analytical approaches (including polymerase chain reaction amplification of 16S rRNA) in similar settings have demonstrated a wide diversity of active bacterial and archaeal assemblages in hydrothermal sediments [5]. Cell counts and measurements of metabolites may not, therefore, yield a complete record of prokaryotic reaction rates and metabolic turnover [6,7]. Hence, our current understanding of the activity of specialised hydrothermal sediment prokaryotic communities remains limited.

Fe-oxides and oxyhydroxides are the major oxidised component of hydrothermal deposits at seafloor vent sites [8]. Sulfide alteration within submarine metalliferous sediments has been compared with subaerial supergene processes [9,10], where in addition to inorganic oxidation processes, morphological evidence suggests that microbial activity plays a significant role in the formation of hydrothermal Fe-oxide deposits [11]. This hypothesis is supported by compelling evidence from in situ incubations combined with 16S rRNA, fluorescent in situ hybridisation (FISH) and cultures of Fe-oxidising bacteria from a variety of hydrothermal settings [12–15]. Microbial activity dominates Fe^{2+} oxidation under low pH conditions where inorganic oxidation is kinetically limited (e.g., subaerial acid mine drainage) and may also play an important role in the formation of hydrothermal Fe-oxide deposits under circumneutral pH conditions [12–14]. However, it has proved difficult to determine the function and impact of specific prokaryotic activity in the wide range of natural hydrothermal settings.

Sediments surrounding hydrothermal mounds contain collapsed sulfide chimney material juxtaposed with oxic substrates [16], creating sharp chemical and physical gradients that generate a range of habitats suitable for prokaryote exploitation. We hypothesise that maximum prokaryotic activity occurs in localised redox zones associated with in situ sulfide alteration. Rapid turnover of redox sensitive species within these microzones limits the impact on pore fluid chemistry and cell counts, but may play a significant role in the fate of hydrothermal deposits on the seafloor. This study combines mineralogical and stable isotope investigation with lipid biomarker analyses, with the aim of studying the impact of prokaryotic metabolism on the mineralogy and geochemistry of hydrothermal sediment undergoing seafloor alteration.

2. Geological setting and *Alvin* zone sediments

The *Alvin* zone is a discontinuous, elongate group of inactive sulfide mounds ~2 km long (NE–SW) by 1 km wide (NW–SE) and is located 2–4 km NNE of the active TAG mound at water depths of 3400–3600 m on the Mid-Atlantic Ridge [17] (Fig. 1). The sediment cores studied here were taken from the southernmost of these mounds (the *Alvin* mound). This mound is ~200 m in diameter and 28 m high, and is similar in size to the nearby active TAG mound [18]. However, heat flow and temperature across the mound are at background levels [19,20], indicating that there is no active venting on the *Alvin* mound at present. Although radiometric dating of massive sulfides from the *Alvin* mound yields an age of ~50 ka [21], there may have been subsequent hydrothermal activity.

The mounds are covered by standing and toppled chimneys, layered hydrothermal crusts and metalliferous sediments intermixed with carbonate-rich pelagic sediment. Samples from the mound top and flanks contain coarse-grained pyrite with minor chalcopyrite and trace amounts of sphalerite [19]. The presence of atacamite coatings and crusts are indicative of Cu leaching from underlying sulfides and local supergene alteration [19,22]. The mounds are undergoing active erosion, mass wasting and dissection by faulting, and are now covered by a heterogeneous layer of Fe-oxyhydroxides [23].

The upper 25–50 cm of sediment on the *Alvin* mound is comprised of oxic metalliferous pelagic carbonate that represents ~10–30 ka of pelagic sedimentation [20,24]. Below this layer, the cores contain sulfidic material derived from mass wasting of mound material mixed with plume particle input from the overlying water column [25]. Oxidation of the sulfides within the sediment has led to complete consumption of dissolved O_2 from the sediment pore water and generation of suboxic–anoxic conditions ~50 cm below the sediment–water interface [3]. There is a minor, but constant, background sedimentation of continental and biogenic material to the area [24], which also undergoes suboxic diagenesis and alteration within the sediment [20]. Net microbial reactions are inferred to be limited by the low organic carbon

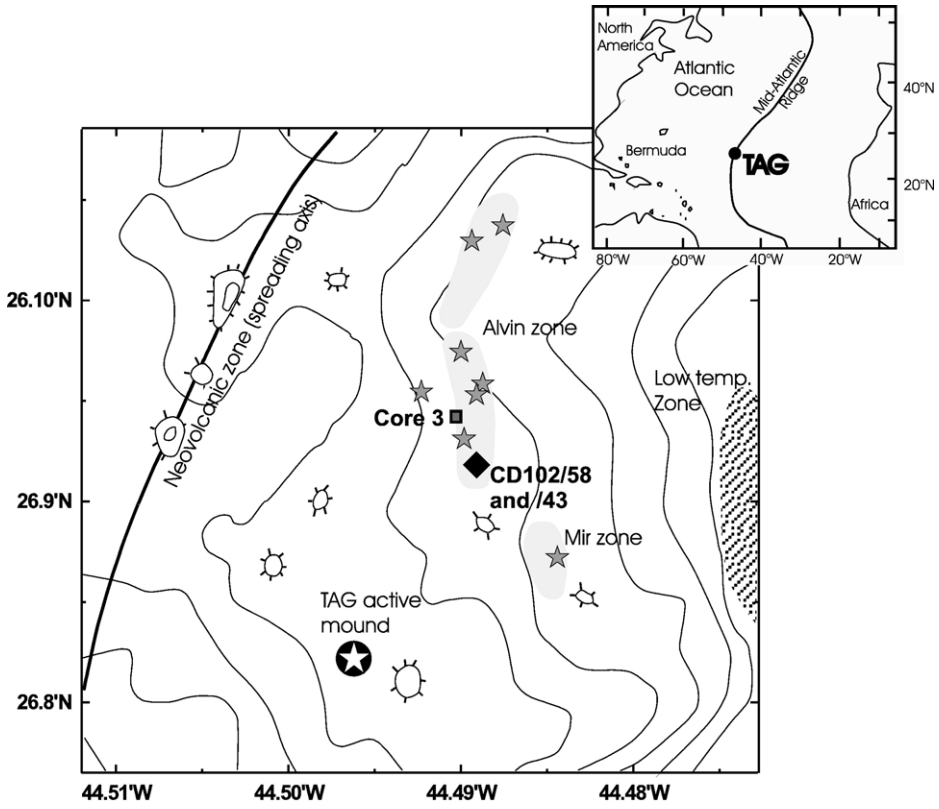

Fig. 1. Map of the TAG hydrothermal field showing areas of sulfide accumulation (active and inactive) and core locations discussed in text (CD102/43 and CD102/58).

input in this setting and overall prokaryote abundance and activity is low [3].

3. Sampling and methodology

Two ~2 m gravity cores: CD102/43 and CD102/58 (26°09.26′N, 44°48.90′W), were collected from the southern periphery of the *Alvin* mound during cruise CD102 of the RV Charles Darwin [26]. A background pelagic core (CD102/10) was also retrieved for direct comparison of deep-sea microbial abundances [3]. Coring was carried out within a 4-receiver transponder net, with a further transponder mounted 25 m above the corer. Navigation records indicate that core 58 was taken ~35 m due north of core 43 [26]. The cores were logged and sampling was based on visual identification of sulfide horizons within the core. Core 43 was sampled for pore waters, solid phase and microbial abundance immediately after recovery on board the ship [3], whereas core 58 had been stored as whole round core at in situ temperature (~4 °C) before sampling for mineralogical, geochemical and organic biomarker investigations. We present new data for core 58 and compare these with published microbial and pore fluid data for core 43 where the methodology has already been described [3].

An overview of the bulk mineralogy and identification of clay separates was carried out by XRD using standard methods [20]. Polished thin sections were prepared for transmitted light microscopy and scanning electron microscopy (SEM) analysis from a resin impregnated laminated section at 76–87 cmbsf. SEM analysis was carried out on a LEO1450VP, W-filament SEM at 20 kV, using a beam current of 80 nA and a probe current of 700 pA. Down core elemental abundance data was determined by ICP-AES using standard methods [3]. $CaCO_3$ content was calculated from the Ca abundance.

Pure sulfide and gypsum mineral separates were obtained by handpicking sediment from depths of 76–100 cmbsf and cleaned via ultrasonication before analysis. Sulfur isotopes were analysed using standard analytical methods [27]. Analyses of international standards NBS-123 and IAEA-S-3, and the SUERC standard CP-1 yielded $\delta^{34}S$ values of +17.1‰, −3.1‰ and −4.6‰, respectively (1σ S.E.<±0.3‰).

Data are reported relative to the Vienna Canon Diablo Troilite (V-CDT) standard.

Three ~10 g sediment samples from the immediate vicinity of the oxide–sulfide boundary in core 58 (74.5, 78.5 and 83 cmbsf) were extracted via a Soxhlet apparatus using dichloromethane–methanol (DCM–MeOH, 2:1 v/v) for 24 h. Total lipid extracts were concentrated using rotary evaporation and a mixture of three standards (androstane, hexadecan-2-ol, hexadecyl-1-octadecanoate) was added. Subsequently, aliquots of all samples were separated into three fractions using a column packed with (activated) alumina by elution with hexane/DCM (9:1 v/v, 3 ml, "apolar fraction") and DCM/MeOH (1:1 v/v, 3 ml, "polar fraction").

Gas chromatography (GC) was performed on a Hewlett Packard 5890, equipped with an on-line injector. A fused silica capillary column (50 m × 0.32 mm) coated with CP-Sil-5 (film thickness 0.12 μm) was used with H_2 carrier gas and the effluent was monitored by a flame ionisation detector. The samples were injected at 50 °C and the oven programmed to increase temperature to 130 °C at 20 °C/min, and then at 4 °C/min to 300 °C, and then held isothermal for 20 min. GC/MS was performed using a Thermoquest Finnigan TRACE GC, equipped with an on-column injector and with He as the carrier gas, interfaced to a Thermoquest Finnigan TRACE MS operated with electron ionisation at 70 eV and scanning a mass range of *m*/*z* 50–700 using a cycling time of 1.7 scan/s. The interface was set to 300 °C with the ion source at 240 °C. The same columns, column conditions and temperature program were used as in the GC analyses. Compounds were identified by comparison of mass spectra and retention time with those reported in the literature.

4. Results

The stratigraphy and geochemistry of core 43 have been described in detail [3,20] and are broadly similar to core 58. Both cores contain a surface layer of pelagic carbonate that varies in thickness across the *Alvin* zone as sediments are redistributed in the rough topography of the median valley [16]. The significant post depositional sediment redistribution and carbonate dissolution preclude any precise estimates of stratigraphic age within these cores.

Below the carbonate cap (52 cmbsf in core 58, 37.5 cmbsf in core 43), the sediment outside the sulfide-rich horizon (76–138.5 cmbsf in core 58, 52.5–57.5 cmbsf in core 43) is dominated by Fe(Mn)-oxyhydroxides including goethite and quartz. Alignment of oxidised elongate clasts in core 58 and minor layering indicates deposition of the sulfide layer via mass flow events, in accord with observations of the distribution of sulfidic material in adjacent cores [3,16]. In core 58, between 76 and 87 cmbsf, the sediment is laminated with alternating

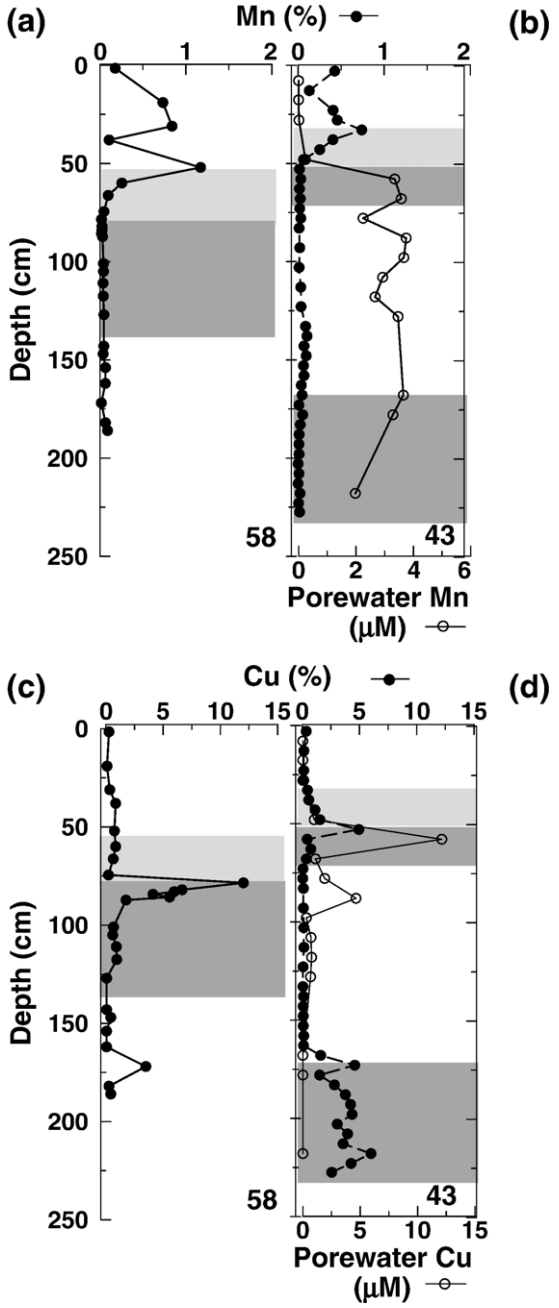

Fig. 2. Downcore variation of (a) solid phase Mn in core 58, (b) solid phase and pore water Mn for core 43, (c) solid phase Cu for core 58 and (d) solid phase and pore water Cu for core 43 (core 43 data are from [3]). Dark grey shading indicates sulfide rich horizons and light grey shading indicates the redox transition zones with suboxic characteristics as defined by redox sensitive metal distribution (see text).

black, sulfide-rich and orange, goethite-rich layers typically ~7 mm thick. The sulfide layers in the laminated section are graded, suggesting sedimentation via small turbidites. This laminated section is underlain by sulfidic material also derived from mass wasting events.

Cores 43 and 58 are both Fe-rich (11–42 wt.% Fe) with transition metal enrichments throughout [3]. Solid phase Mn contents are elevated in the upper portion of all cores in the TAG area [24,28–32] with Mn contents within the carbonate cap of cores 43 and 58 of 0.1–1.2 wt.% (Fig. 2a and b). Pore fluid $Mn(II)_{aq}$ levels are below detection limit in the upper part of core 43 and only reach significant levels below ~50 cmbsf, which is inferred to represent the boundary between oxic and suboxic sediment (Fig. 2b; [3]). Solid phase Cu levels are relatively low in the carbonate cap, but are significantly elevated (up to 12 and 5 wt.% in cores 58 and 43, respectively; Fig. 2c and d) at the top of the sulfide layer, which is co-incident with the depth of the pore water $Mn(II)_{aq}$ maximum. Pore fluid Cu levels are negligible in core 43, except in and immediately below the sulfide layer (12 and 4 μM, respectively [3]; Fig. 2d).

The solid phase Mn and Cu distribution in the two cores is used to correlate sulfide horizons and allow direct comparison of redox driven processes across the coring sites (Fig. 3a, b, d and e). Thus, the redox sensitive metal distribution is used as a proxy for O_2 penetration ($Mn(II)_{aq}$ mobilisation only occurs in suboxic conditions in submarine sediments) and all data are presented relative to the depth of the well-defined Cu-rich horizon (assigned a zero depth) throughout the ensuing sections. The carbonate content in both cores decreases from pelagic values (25–30%) at the top of the redox transition zone to negligible levels at the supergene reaction front (Fig. 3c and f).

4.1. Mineralogy

Pyrite is ubiquitous in the sulfidic portion of both cores and locally constitutes up to 75% by volume, where it occurs as both a primary hydrothermal mineral (although transported from its original deposition site) and a secondary mineral associated with later alteration. Primary pyrite is most commonly present as fine- to medium-grained aggregates of euhedral cubes and less commonly as: (1) reworked, randomly orientated, collomorphic crusts and spheres; (2) medium- to coarse-grained singular euhedral cubes; and (3) tube-like structures. Oxidative corrosion and dissolution of primary pyrite is indicated by the presence of irregular grain boundaries, enclosed by layered or filamentous Fe-oxide and dissolution pits on grain surfaces frequently filled with secondary

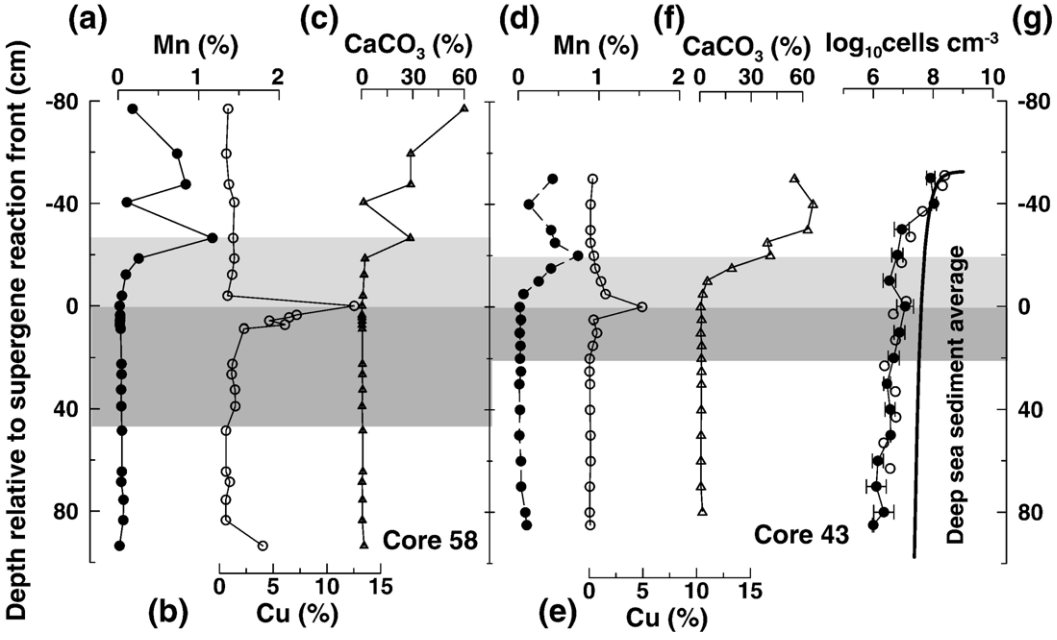

Fig. 3. Comparison of the solid phase (a) Mn, (b) Cu and (c) $CaCO_3$ distribution against depth relative to the Cu rich horizon in core 58; and the (d) Mn, (e) Cu and (f) $CaCO_3$ distribution in core 43; and (g) $\log_{10}$ cell numbers cm^{-3} sediment in core 43 (closed circles) and a pelagic background core from the MAR (open circles). The solid line represents the mean value for low organic carbon (<1%) deep-sea sediments [3]. Shading as for Fig. 2.

minerals—most commonly, Fe-oxides and Fe-oxyhydroxides with minor Fe-silicates.

Almost all chalcopyrite within core 58 is paragenetically early, and transported to the sediment from its original high temperature precipitation site. It is largely concentrated in a layer 2.5–8.5 cmbrf (cm below the supergene reaction front) where its abundance ranges from 5% to 20% by volume. Below this zone, chalcopyrite becomes increasingly sporadic. In general, chalcopyrite occurs as sub-anhedral, medium-grained crystals, but it also occurs as rare sub-euhedral singular grains and aggregates; these are typically secondary and in many cases indicate co-precipitation with secondary pyrite. In rare cases, chalcopyrite is observed as an overgrowth on primary pyrite cubes. All primary chalcopyrite grains show evidence of alteration, most frequently seen as corrosion of grain boundaries, dissolution pitting, covellite rims and fracture cements, as well as replacement by porous covellite. In addition, partial replacement by and overgrowth rims of sphalerite and pyrite are relatively common.

Covellite (CuS) within core 58 is an alteration product of chalcopyrite and although it is concentrated in the layer 2.5–8.5 cmbrf (Fig. 2c), it is also present throughout the sulfidic layer. Covellite typically occurs as porous, anhedral grains replacing chalcopyrite, but it is also present as collomorphic crusts. Atacamite ($Cu_2Cl(OH)_3$) and paratacamite (a polymorph of atacamite) are secondary Cu phases and their abundance mirrors that of chalcopyrite and covellite, but the former are also enriched at 0 cmbrf.

Late stage gypsum ($CaSO_4{\cdot}2H_2O$) occurs as occasional medium- to coarse-grained euhedral crystals with abundant Fe-oxide/oxyhydroxide and pyrite inclusions. Gypsum is distributed across the oxic–suboxic boundary between −10.5 and 38.5 cmbrf. The Fe-oxide and oxyhydroxide inclusions have filamentous morphologies (Fig. 4a and b), whereas the included pyrite is typically euhedral. Gypsum cross-cuts silica and goethite layers and clasts and indicates that gypsum was paragenetically late within these sediments (Fig. 4). (Note, although gypsum precipitation can form during core storage through sulfide alteration [33], this generates large idiomorphic crystals that form overgrowths on all phases. In contrast, the gypsum within core 58 is space filling (Fig. 4) and closely associated with the supergene mineral assemblage (atacamite–covellite–gypsum) and is thus an original feature of the sediments and not a post-coring artefact.)

Clay minerals constitute an average of 7% by volume of the bulk sediment within core 58 (cf. 11–64% in core 43; [20]), but the clay content of the sulfide layer and overlying transition zone is very low in both cores (<1%). XRD analyses indicate that the clays are almost exclusively smectite, with trace amounts of illite. Based on comparison with core 43 [20], the smectites are inferred to be low temperature hydrothermal nontronites ($NaFe_2(Si,Al)_4O_{10}(OH)_2{\cdot}H_2O$).

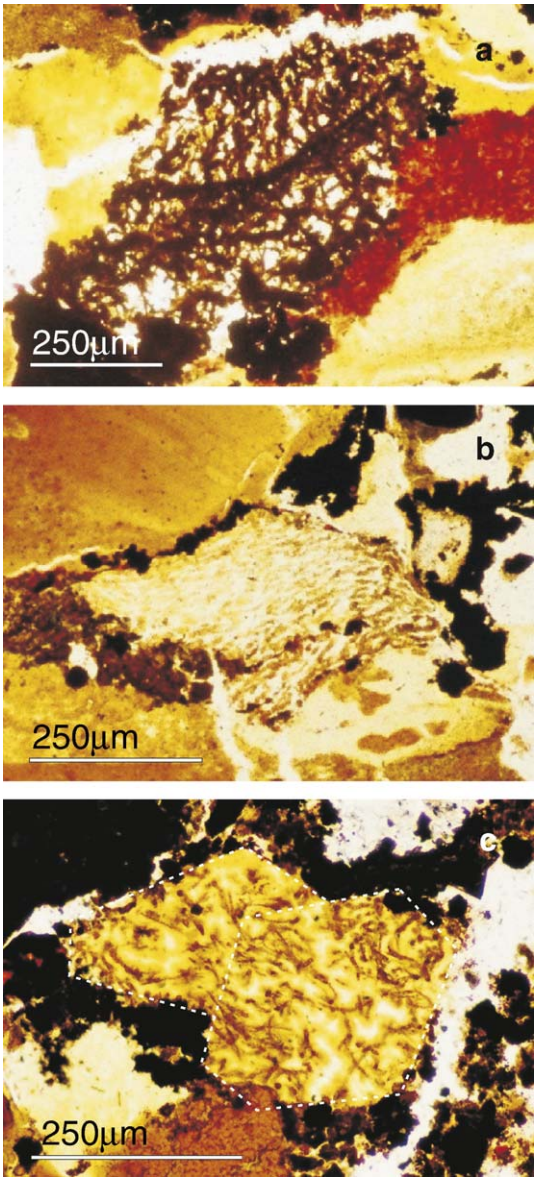

Fig. 4. Transmitted light photomicrographs of filamentous structures cemented by gypsum. (a) Dendritic mass of Fe oxide filaments within euhedral gypsum crystal; (b) goethite filaments showing directed growth lengthwise parallel to sedimentary layering; (c) rod-like goethite filaments variably encrusted with hematite cemented by twinned euhedral gypsum crystals. White dashed lines indicate the crystal boundaries.

Well-preserved haematite and goethite filaments occur throughout the goethite and quartz dominated layers in the laminated sulfide section of core 58 (−2.5 to 8.5 cmbrf) and are associated with the secondary mineral assemblage of silica, gypsum, secondary pyrite, covellite, atacamite and goethite. The filaments range in diameter from ~0.5 to 10 μm and are typically 50–100 μm long, but can be up to 250 μm in length. They occur enclosed within gypsum (Fig. 4a–c) and amorphous silica and quartz phases (Fig. 5a–d), and also occur as non-cemented filament meshes of interlocking, rod shaped, branched and dendritic filaments that are exclusively associated with and surrounding corroded pyrite grains (Fig. 6a and b).

4.2. Isotope geochemistry of sedimentary minerals

Sulfur isotope data for sulfide and sulfate phases in core 58 are presented in Table 1. The $\delta^{34}S$ values of bulk sulfide samples fall within a narrow range (+6.9‰ to +8.3‰; Fig. 7), with a mean value of +7.6±0.5‰ (1σ, n=8). Gypsum also has a restricted range of $\delta^{34}S$ values from +9.6‰ to +10.6‰, with a mean of +10.0±0.4‰ (1σ, n=7) (Fig. 7).

4.3. Lipid biomarkers at the redox front

Polar compounds are either absent or present in trace amounts, but the apolar fractions contain abundant and variable compound assemblages. The apolar fractions from each sample (−4 cmbrf: redox transition zone, 0 cmbrf: supergene reaction front and +4.5 cmbrf: sulfide zone; Fig. 8) contain diverse hydrocarbons, including *n*-alkanes, branched alkanes, biphytanes, steranes and hopanes. The sterane distributions in each sample are similar and are characterised by a predominance of C_{27} (cholestane) components, with subordinate C_{29} (24-ethylcholestane) and trace C_{28} (24-methylcholestane) (Fig. 8; *m*/*z* 217 traces). All three samples exhibit a thermally mature distribution of steranes (with respect to alteration of the inferred original stereochemistry; e.g., [34]). However, the redox transition zone (−4 cmbrf) sample contains a higher proportion of 13β,17α(*H*) diasteranes. The hopanes show similar behaviour (Fig. 8; *m*/*z* 191 traces): all samples contain a similar distribution of hopanes with respect to their carbon numbers, but the

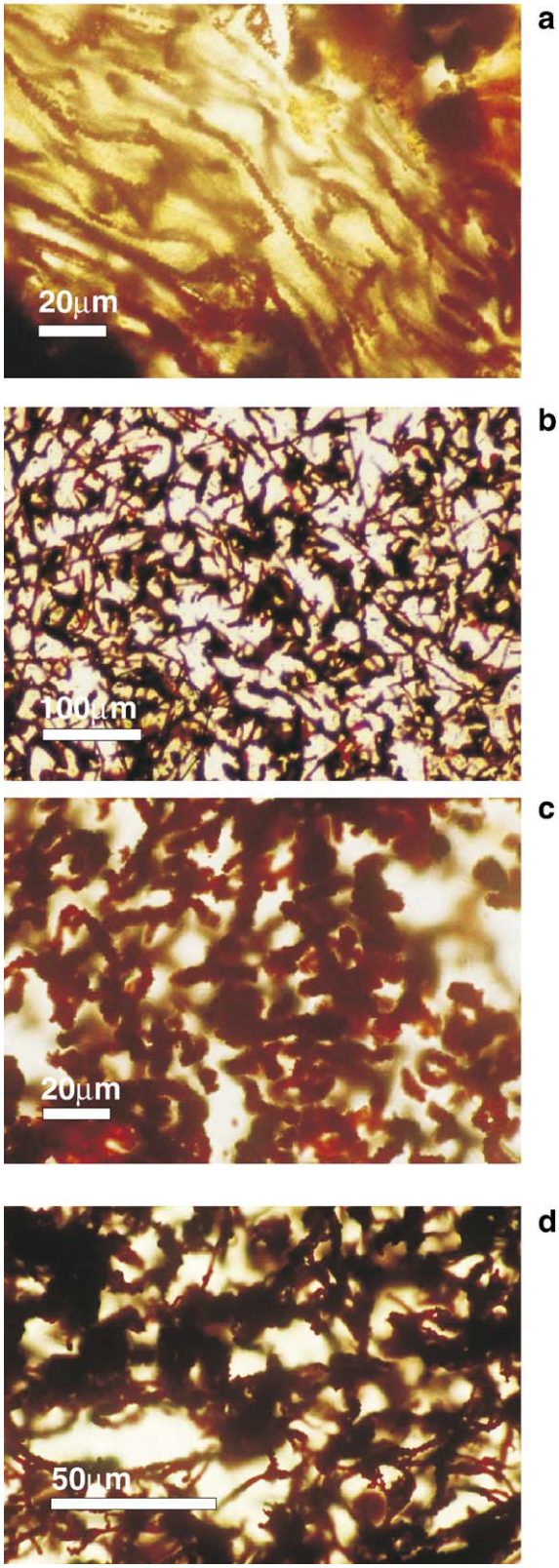

Fig. 5. Transmitted light photomicrographs of filamentous structures cemented by silica. (a) Long twisted goethite filaments showing directed growth lengthwise parallel to sedimentary layering; (b) rod-like hematite filaments; (c) bundled twisted filaments; (d) mesh of twisted and rod-like filaments some show branching.

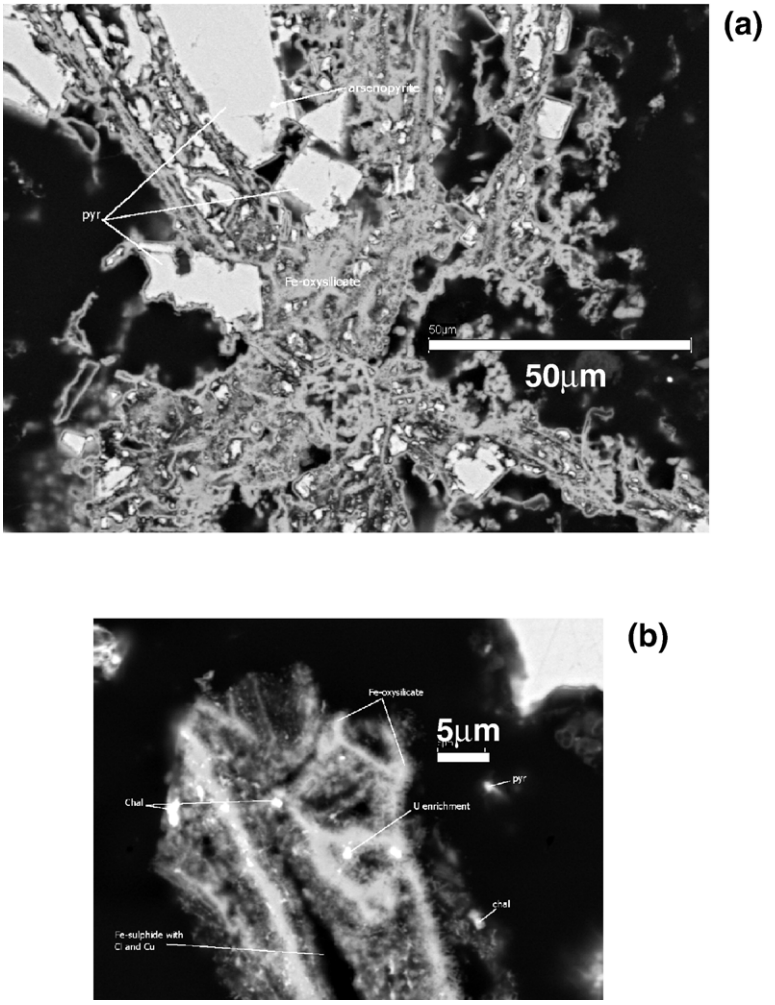

Fig. 6. SEM images of Fe oxide filaments encrusted by Fe silicates and amorphous silica associated with sulfide surfaces. (a) Branching filament network growing around sub-euhedral pyrite grains and (b) branched filaments embedded within Fe-oxides and amorphous silica.

redox transition zone sample has a more altered distribution, reflected by the absence of 17β(*H*),21α hopanes (Fig. 8b). In addition, both hopanes and steranes are much less abundant in the redox transition zone sample than in the supergene reaction front and the sulfidic samples (Fig. 8b).

All three samples contain a range of branched alkanes (Fig. 8). Alkane distributions are similar in the supergene reaction front and the sulfidic samples. In these samples, almost all of the compounds exhibit spectra similar to those generated by *n*-alkanes, i.e., a sequence of fragment ions characterised by an increasing number of methylene units (*m*/*z* 57, 71, 85, 99, etc.) and are therefore apparent in the *m*/*z* 57 mass chromatogram as well as the total ion current (Fig. 8a). However, co-injection with an *n*-alkane-rich extract reveals that the supergene reaction front and the sulfidic samples contain few *n*-alkanes, which are subordinate in abundance except in the higher molecular weight portion of the chromatogram. Instead, the majority of the compounds appear to be simple methyl-branched alkanes, for which strict structural determination was not possible.

In contrast, the redox transition zone sample (−4 cmbrf) contains predominantly *gem*-diethyl alkanes, in which the ethyl substituents are at the same carbon atom resulting in multiple homologous series of quaternary-branched compounds (Fig. 8b; TIC and *m*/*z* 127 trace). These are dominated by the 5,5-diethyl components, but a variety of other series are present in subordinate abundances (data not shown). Also abundant in this sample are series of *n*-alkylcyclopentanes, *n*-cyclohexanes and tentatively identified *n*-alkylcycloheptanes.

5. Discussion

Oxygen penetration into Cu-bearing hydrothermal sediments leads to oxidation of pyrite and chalcopyrite, a decrease in pH and Cu mobilisation and re-precipitation at the supergene reaction front (Figs. 2 and 3; [35]). This generates a peak in solid phase Cu (as a combination of atacamite and secondary Cu-sulfides) that can be used to track the penetration of oxygen into the sediment (Fig. 3a–f). The depth interval above the supergene reaction front, between the Mn and Cu solid phase peaks, represents a transition zone where there is significant redox cycling of Mn, Cu and other transition metals (Fig. 2a–d).

5.1. E_h–pH conditions during diagenesis

Supergene enrichment of metals in metalliferous sediments exposed to subaerial weathering has been ascribed to a two-stage process [36]. (1) Sulfides undergo oxidation, producing acidic pore waters that lead to mineral dissolution and transport of metals. Fe-oxide and Fe-oxyhydroxides are precipitated in the leached zone to form a gossan cap, while metal-bearing solutions diffuse downwards. (2) Below the redox front, the leached metals are re-precipitated in secondary minerals. These reactions typically involve replacement of primary sulfide minerals by secondary sulfides; for example the conversion of chalcopyrite to covellite [36]. The mineral assemblage observed in association with the redox and pH front in *Alvin* zone sediments (covellite–secondary pyrite–gypsum–atacamite) is a typical acidic supergene alteration assemblage commonly associated with Cu ore bodies [37,38].

Table 1
Sulfur isotope data for sulfide and gypsum phases from core CD102/58

Depth below sea floor (cmbsf)	Depth below supergene reaction front (cmbrf)	$\delta^{34}S_{sulfide}$ (‰)	$\delta^{34}S_{gypsum}$ (‰)
75.75	−2.75		+10.4
76.25	−2.25		
77.50	−1.00	+7.0	+9.7
78.00	−0.50		
79.50	1.00		+10.0
80.75	2.25	+6.9	
81.50	3.00		
82.50	4.00		
83.00	4.50	+7.6	+9.9
85.00	6.50	+7.6	+9.9
91.00	12.50		+9.6
93.00	14.50	+8.3	
97.00	18.50	+7.9	
99.00	20.50		+10.6
103.00	24.50	+7.3	
109.00	30.50	+7.9	

Analytical error on $\delta^{34}S$ is ±0.3 ‰ (1σ).

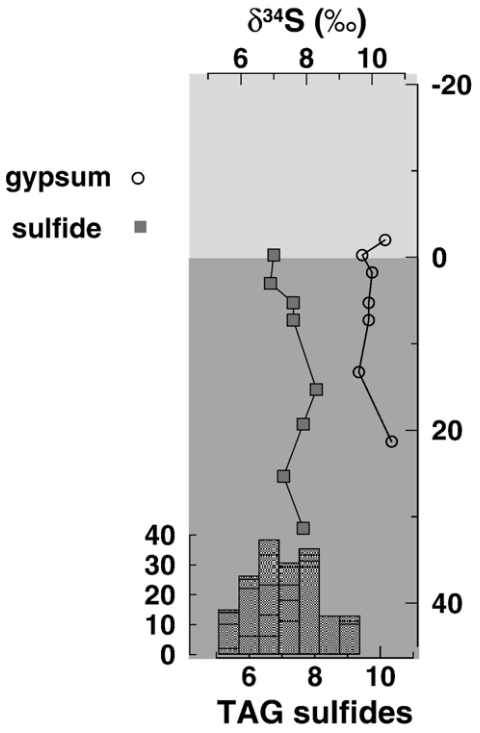

Fig. 7. Down core variation in $\delta^{34}S$ for gypsum and sedimentary sulfides. Light grey shading represents the transitional redox zone. Bar chart shows literature data for TAG active mound sulfides for comparison [54,57].

The evolution of the redox conditions during diagenesis can be summarised by comparing the mineralogy and pore water geochemistry with E_h–pH diagrams (Fig. 9). The initial sediment composition is assumed to be sulfide minerals (principally pyrite, with lesser amounts of Cu- and Zn-sulfide) that were emplaced during a mass flow event. The temperature is assumed to have been close to bottom water, i.e., ~2 °C. Initial oxidation of the sulfide produces acid conditions through reactions such as:

$$FeS_2 + 3.5O_2 + H_2O \Leftrightarrow Fe^{2+} + 2H^+ + 2SO_4^{2-} \quad (1)$$

$$2FeS_2 + 7.5O_2 + 4H_2O \Leftrightarrow Fe_2O_3 + 8H^+ + 4SO_4^{2-} \quad (2)$$

Pore water concentrations of $Fe(II)_{aq}$ reach 33 µmol/l at the redox front in core 43 [3], which suggests that reaction (1) is predominant in these sediments though some haematite filaments are seen in core 58 associated with Fe-oxide filaments (Figs. 4c and 5b). Acidic

conditions are also implied by pore water measurements (pH = 3.5–5.5) from sulfidic cores from the active TAG mound [39,40]. These conditions would also lead to the partial oxidation of chalcopyrite to covellite or bornite:

$$CuFeS_2 + 2O_2 \Leftrightarrow CuS + Fe^{2+} + SO_4^{2-} \quad (3)$$

$$5CuFeS_2 + 11O_2 + 2H_2O \Leftrightarrow 4H^+ + 4Fe^{2+} + 6SO_4^{2-} + Cu_5FeS_4 \quad (4)$$

However, the absence of bornite in sediments from core 58 suggests that reaction (3) is dominant and that the initial E_h–pH conditions lie within Box 1 in Fig. 9 (i.e., pH ~ 4). The porous texture of the covellite within core 58 indicates that it has undergone retrograde dissolution, suggesting that conditions became more oxidising:

$$4CuS + 7O_2 + 2H_2O \Leftrightarrow 4Cu^+ + 4SO_4^{2-} + 4H^+ \quad (5)$$

The presence of Fe-oxide filaments within the sulfide zone indicates that reactions such as the formation of goethite were also occurring:

$$O_2 + 4Fe^{2+} + 6H_2O \Leftrightarrow 4FeOOH + 8H^+ \quad (6)$$

Both of these reactions ((5) and (6)) produce protons and suggest that conditions became increasingly acidic. The Fe-oxide assemblage (dominated by goethite and amorphous oxyhydroxides, coupled with the absence of jarosite) indicates relatively well buffered system compared with acid mine drainage. Additionally, atacamite is abundant within the sulfide zone and it has a limited stability field that does not extend to low pH (Fig. 9). Hence, the presence of high levels of dissolved Mn^{2+} in pore waters of the sulfide zone and active redox front together with atacamite means that the E_h–pH conditions must evolve in the direction of Box 2 in Fig. 9 (i.e., pH ~ 7–9). As with the reactions above, precipitation of atacamite also produces protons:

$$4Cu^+ + 2Cl^- + O_2 + 4H_2O \Leftrightarrow Cu_4(OH)_6Cl_2 + 2H^+ \quad (9)$$

Indeed, all the reactions identified above produce protons, but Fig. 9 shows that atacamite is unstable at low pH. Hence, the acidity generated during Fe and Cu diagenesis must be neutralized, most probably via carbonate dissolution in the redox transition zone. Sedimentary textures indicate that gypsum and atacamite precipitation were either contemporaneous with one another or, in some cases, atacamite formation predates precipitation of gypsum. The upper temperature limit of circulating fluids is thus constrained by the atacamite E_h–pH stability field, which shrinks with increasing temperature, and effectively disappears above 50 °C. Oxygen isotope geothermometry of nontronites indicate that circulation of 54–64 °C fluids were pervasive in nearby core 43 [20]. This suggests that atacamite formation at the redox front in core 43 may postdate nontronite formation at this site.

5.2. Prokaryote abundance and Fe-oxide morphology

The numbers of prokaryotic cells are extremely low at this hydrothermal site (Fig. 3g) but are comparable with background pelagic sediments from similar latitudes and depth [3]. There is a statistically significant increase in cell numbers at the limit of O_2 penetration or supergene reaction front where the prokaryotic numbers within the sulfide layer are approximately double those within the redox transition zone or the deeper oxyhydroxides [3]. This zone of prokaryote enrichment coincides with the depth of maximum Fe-oxide filament occurrence within the supergene mineral assemblage.

The Fe-oxide filaments observed in this study (Figs. 4–6) share many morphological characteristics with Fe-oxide filaments described from previous studies of seafloor hydrothermal deposits, and are similar to filaments observed in terrestrial jasper deposits [11]. Some of the filament morphologies can be directly compared to known Fe-oxidising microbes. For example, the twisted filaments (Figs. 4 and 5a, c and d) are similar to the encrusting Fe-oxide twisted stalks of *Gallionella* spp. [8,12,41–44] at seafloor hydrothermal vent sites and weathered sulfide mineral surfaces [13]. Other morphologies illustrated in Figs. 4 and 5 can be compared to the Fe-oxide encrusted sheaths of *Leptothrix* spp. (Fig. 5a; [45]) and to the filamentous structures formed by the novel bacteria strain PV-1 (Fig. 4c; [12]). Branching filaments, which are common at this site (Fig. 5d), may record true branching of filamentous microbes or "false-branching", where there is successive budding of separate microbial cells; a phenomenon known to produce bifurcating stalks in *Gallionella* spp. [46] and sheaths in *Sphaerotilus natans* [47].

Filament occurrence is limited to the redox transition zone and upper sulfide zone and reaches a maximum of ~ 10% of the sediment volume at the supergene reaction front (Fig. 6a). Within this zone, the filament meshes associated with sulfide surfaces reach a density comparable to those observed in experimental incubations on sulfide surfaces (~ 10^8 cells/cm^3; [13]) but the bulk cell abundance is still extremely low compared with other deep-sea sites (Fig. 3g). It is noteworthy that the zone of maximum filament density is coincident

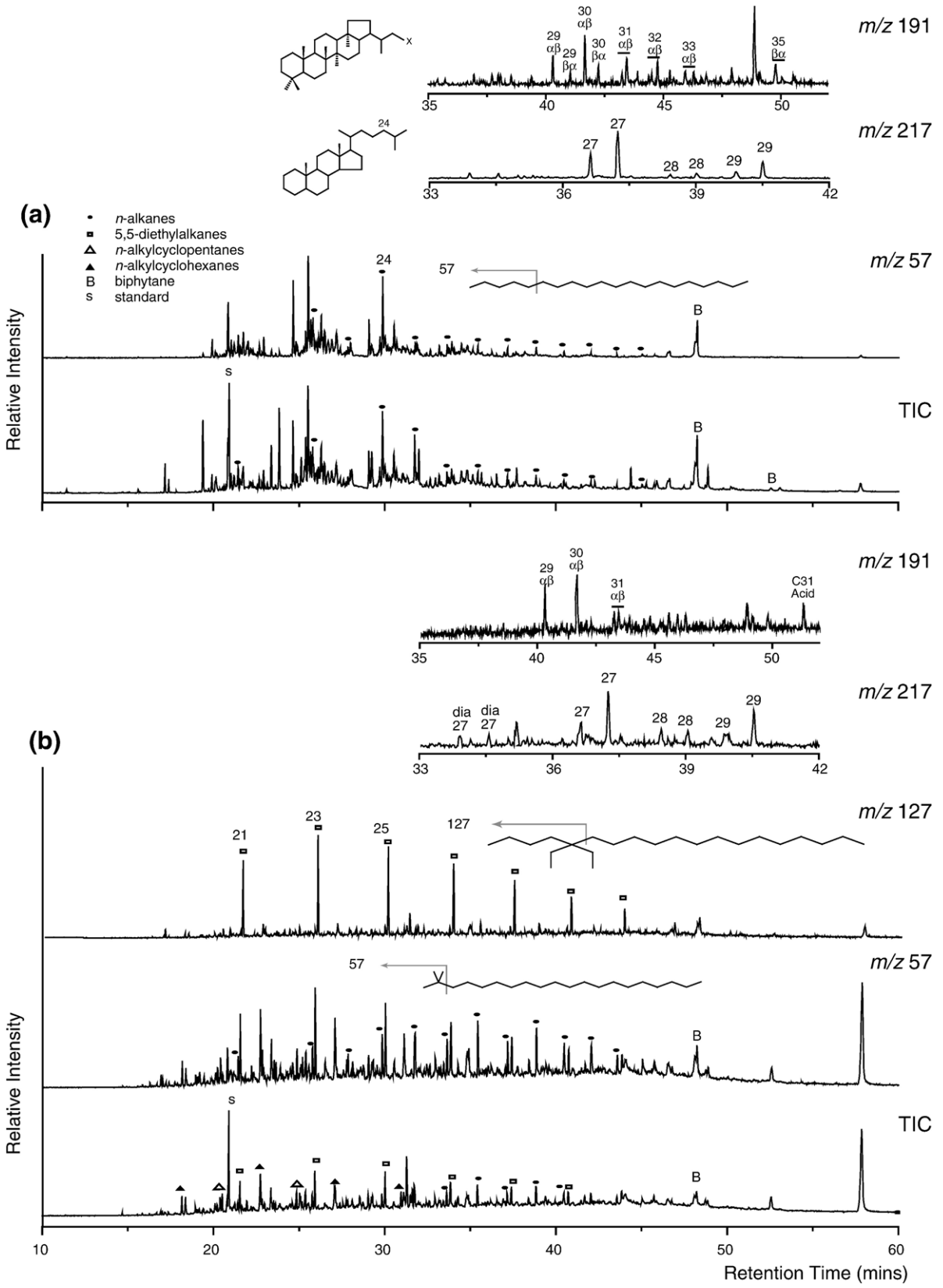
(a)
n-alkanes
5,5-diethylalkanes
n-alkylcyclopentanes
n-alkylcyclohexanes
B biphytane
s standard
m/z 191
m/z 217
m/z 57
TIC
Relative Intensity
(b)
m/z 191
m/z 217
m/z 127
m/z 57
TIC
C31 Acid
dia 27
Retention Time (mins)

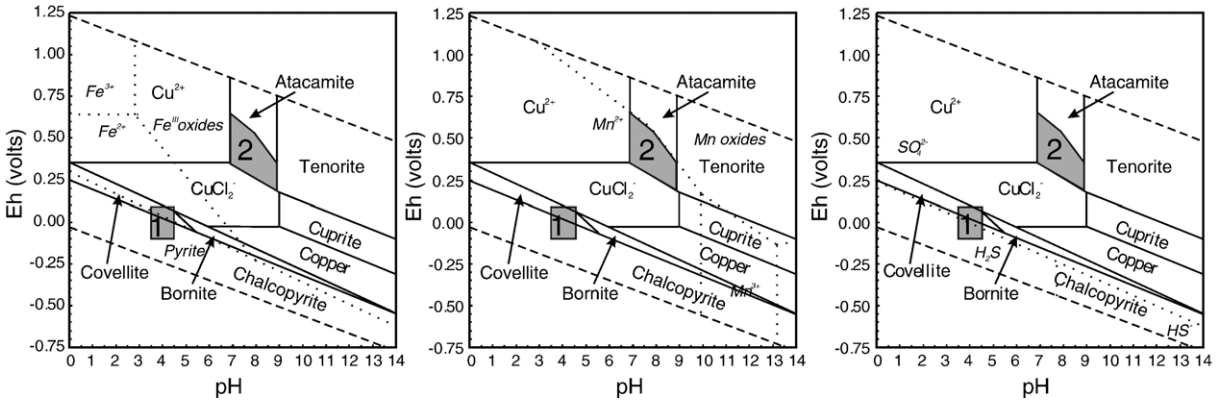

Fig. 9. E_h–pH stability diagrams for copper minerals and dissolved species. Dashed lines show stability field of water. Dotted lines show stability fields for (a) Fe, (b) Mn and (c) SO_4^{2-} species. Major element species are at seawater concentrations, temperature is 2 °C. Dissolved Cu, Fe and Mn concentrations taken from core 43 data [3] and are 5 μmol/l, 30 μmol/l and 4 μmol/l, respectively. These figures were generated using Geochemists Workbench [67].

with the statistically significant doubling in prokaryote cell numbers (Fig. 3g; [3]) and is also the locus of the supergene reaction front.

The large dendritic filaments (Figs. 4a and 5d) are also comparable to dendritic Fe-oxide filamentous textures observed in Fe-oxide-silica deposits in the Indian Ocean [48], East Pacific Rise [49] and active TAG mound [50], although these occurrences were not attributed to microbial strains or morphologies. Rather, they have been attributed to abiotic processes resulting from diffusion limited growth of branching Fe-oxide aggregates in a viscous silica gel generated at a redox front created by pyrite weathering [50]. Two lines of evidence have been used to support this model [50]: (1) any cavities between the Fe-oxyhydroxide dendrites are filled entirely with silica and (2) the dendrites do not project beyond the silica into free space. However, in this study, we observed uncemented dendritic filament meshes and ramified and filamentous dendrites cemented by both silica and gypsum (Figs. 4–6). Hence, we suggest that the filaments observed in the *Alvin* mound sediments are not abiotic diffusive structures, but are biogenic in origin.

5.3. Organic biomarker distribution

The organic biomarker data presented here are generally consistent with previous studies on MAR hydrothermal sediments [51]—i.e., these biomarkers were likely derived from organisms living on the hydrothermal mound rather than the overlying water column. Biphytane (sensu strictu) and biphytane bearing a single cyclopentyl moiety are C_{40} isoprenoids and derive from the membrane lipids of archaea. Steranes derive from sterols that act as membrane rigidifiers in eukaryotes. Hopanes derive from functionalised hopanoids, membrane rigidifiers in some bacteria. Cholesterol is ubiquitous in marine organisms, so the predominance of cholestane is not unusual. The redox transition zone (−4 cmbrf) sample contains a higher proportion of 13β,17α(*H*)diasteranes (sterane structural isomers and diagenetic transformation products), suggesting this sediment was exposed to more acidic or oxic conditions (e.g., [52]). The altered hopane distribution could also could be due to acid or oxygen catalysed transformation to the more stable 17β(*H*),21α isomer. In addition, both hopanes and steranes are much less abundant in the −4 cmbrf sample than in the deeper sediments (Fig. 8b). This is likely a consequence of greater degradation, either by greater post-depositional microbial reworking of organic matter associated with carbonate dissolution or thermal (10–40 °C) alteration.

However, gem-dimethyl and -diethyl alkanes exhibit the most significant abundance and distribution variations through the core. These compounds are abundant in the redox transition zone (−4 cmbrf), but absent in the deeper supergene reaction front and sulfidic samples. The latter observation indicates that the *gem*-dimethyl and -diethyl alkanes are not simply

Fig. 8. Partial total ion currents, *m/z* 57, *m/z* 217, *m/z* 191 and *m/z* 127 (b only) mass chromatograms for (a) the +4 cmbrf sediment horizon and (b) the −4 cmrf cmbsf sediment horizon in core 58. The total ion currents show all compounds present in the fractions, whereas the *m/z* 57 mass chromatograms show *n*-alkanes and branched alkanes. Numbers refer to the total carbon atoms in the compounds.

the result of catagenetic processes but likely reflect differences in the original microbial populations. These compounds derive from unknown organisms, but have been found in recent hydrothermal sediments [51] and ancient sedimentary rocks [53]. Indeed, the same predominance of *gem*-diethyl alkanes, especially the 5,5-diethyl components, has been observed in Rainbow sulfidic sediments [51]. These quaternary-branched alkanes appear to be associated with intense redox boundaries and have been attributed to sulfide-utilising chemoautotrophs; however, this is far from certain and they could be associated with other organisms living at active redox boundaries. The presence of *gem*-diethyl alkanes in the transition zone of the *Alvin* mound sediments–combined with their absence in deeper sediments–provides direct evidence for a novel microbial assemblage in the oxidising sediments. These compounds apparently record a molecular signature of iron or sulfide oxidation under circumneutral conditions based on the evidence from the E_h–pH conditions, mineralogy and geochemistry.

5.4. Sulfur isotope systematics and sulfide alteration

The $\delta^{34}S$ of bulk sulfide samples from this study (+6.9‰ to +8.3‰) fall within the range previously observed for TAG sulfides (Fig. 7; +4.4‰ to +10.3‰, mean +6.9±0.3‰ 1σ, n=233; [54–57]). By comparison, the $\delta^{34}S$ of H_2S in the black smoker fluid from TAG ranges from +6.6‰ to +7.5‰ [57]. These data are 3–4‰ higher than $\delta^{34}S$ values from other sediment-free mid-ocean ridge hydrothermal sites probably due to incorporation and reduction of seawater SO_4^{2-} during mound evolution [58].

Ca^{2+} concentrations in pore waters of the *Alvin* mound are close to seawater values and those of SO_4^{2-} are only slightly elevated, so that gypsum is predicted to be undersaturated [3]; hence, purely inorganic precipitation of gypsum is unlikely. However, meshes of bacterial filaments growing directly from oxidation of mineral dissolution products on sulfide layers could create geochemical microenvironments at mineral-pore water interfaces [59,60]. In this case, free advective and diffusive exchange with bulk pore waters would be restricted and build up of SO_4^{2-} released by sulfide oxidation could lead to local supersaturation of gypsum. The filament surfaces may also act as heterogeneous nucleation sites, thus lowering the saturation level required for precipitation compared to homogeneous abiogenic nucleation from a fluid [61].

The $\delta^{34}S$ of gypsum from core 58 ranges from +9.6‰ to +10.6‰ (Table 1), with the lowest values associated with the locus of supergene alteration (i.e., 0 cmbrf). The equilibrium fractionation $\Delta_{gypsum\text{-}sulfate}$ at seafloor temperatures is ~+1.65‰ [62]. Applying this value to the data presented here suggests that the dissolved SO_4^{2-} in parent fluid for gypsum formation had a $\delta^{34}S$ of +7.9‰ to +8.9‰, which is at and slightly heavier than the upper end of the range observed in bulk sulfides from core 58 (+7.6±0.5‰; Fig. 7). This strongly indicates that sulfur within the gypsum was derived from sulfide oxidation rather than incorporation of seawater SO_4^{2-} ($\delta^{34}S$=+20.9‰; [63]). While is it not possible to distinguish definitively between biologically and abiologically mediated oxidation on the basis of the S isotope data alone, it is not unreasonable to suggest that the coincidence of the unambiguous isotope data indicating oxidation, with the significantly increased prokaryote cell count, is consistent with biological mediation [63]. The isotope data are also compatible with the observation that supergene alteration involves quantitative sulfide oxidation rather than partial oxidation and isotopic re-equilibration [64]. This hypothesis is in marked contrast to observations of sub-seafloor anhydrite associated with active hydrothermal deposition at black smoker sites [54,65], where sulfate sources are dominated by seawater. The S isotope data also demonstrate that anhydrite is not a precursor to *Alvin* mound gypsum.

The supergene mineral assemblage and active sulphide oxidation both imply acidic conditions [66]. Such conditions will lead to carbonate dissolution in the vicinity of the supergene reaction front. Dissolution of the carbonate will neutralise the pore fluid pH allowing circumneutral conditions to prevail—a requirement for distinct populations of Fe-oxidisers to flourish [67]. Thus, while the overall prokaryote counts are extremely low, and generally the pore fluids are acidic and anoxic below the redox front [3], there is significant circumneutral Fe oxidation within the redox transition zone and the supergene reaction front.

6. Conclusions and wider implications

There is a specialized prokaryote community present in hydrothermal sediments with low total cell numbers, although a significant stimulation of activity (doubling of cell counts) is associated with active redox fronts [3]. This stimulation is manifest as unusual quaternary-branched hydrocarbon biomarkers and dense Fe-oxide filament occurrences associated with supergene alteration products in the shallow subsurface of the

hydrothermal mound. These filaments served, in turn, as nuclei for formation of late stage gypsum, which is unambiguously identified as a sulfide oxidation product. Sulfur isotope measurements on hydrothermal sediment sulfide and the late sulfate phase demonstrate that this gypsum is unambiguously derived from quantitative sulfide oxidation with negligible seawater sulfate contribution, which, together with the enhanced prokaryotic activity, suggests a likely role of biologically induced mineralisation.

Redox sensitive metal distributions, particularly Cu and Mn, can be used as stratigraphic markers of the active redox front and transition redox active zone in hydrothermal settings. Net microbial reaction rates inferred from metabolic product distribution are low [3] but intense cycling occurs within a narrow transition zone at the redox interface driven by sulfide oxidation and neutralization by carbonate dissolution. Sulfide alteration in hydrothermal sediments is likened to subaerial supergene processes. In contrast to the much larger scale, downward migrating zones of oxidation and secondary enrichment observed in sub-aerial deposits, submarine supergene processes appear to be dominated by locally important, grain-scale re-mineralisation and secondary enrichments.

These new data demonstrate that, in order to gain a full understanding of the processes controlling the alteration of seafloor hydrothermal sites, it is important to carry out microscale mineralogical, microbiological and textural studies in addition to geochemical and isotopic analyses to unravel the complex paragenetic sequences of sulfide precipitation and alteration. This study has provided new insights into the inferred, but rarely proven influence of prokaryotes on the supergene alteration of submarine hydrothermal sulfide mounds.

Acknowledgements

We are grateful to captain and crew of RRS Charles Darwin for their assistance during the BRIDGE Cruise CD 102. Particular thanks to B. Cragg and J. Parkes for useful discussions, and M. Rudnicki and J. Rhodes for help with shipboard and other analyses. R. Jones, J. Ford and R. Pearce are thanked for help with sample preparation. We also thank B. van Dongen for performing organic geochemical analyses, and I. Bull and R. Berstan for technical support. This research was funded by the Natural Environment Research Council, UK, BRIDGE Programme and NERC studentship GT4/00/247 to SG. SUERC is supported by NERC and the Scottish Universities. AJB is funded through NERC support of the Isotope Communities Support Facility at SUERC. The manuscript benefited greatly from the comments from two anonymous reviewers.

References

[1] R.J. Parkes, B.A. Cragg, P. Wellsbury, Recent studies on bacterial populations and processes in subseafloor sediments: a review, Hydrogeol. J. 8 (2000) 11–28.

[2] A. Schippers, L.N. Neretin, J. Kallmeyer, T.G. Ferdelman, B.A. Cragg, R.J. Parkes, B.B. Jorgensen, Prokaryotic cells of the deep sub-seafloor biosphere identified as living bacteria, Nature 433 (2005) 861–864.

[3] S. Severmann, R.A. Mills, M.R. Palmer, J.P. Telling, B.A. Cragg, R.J. Parkes, The role of prokaryotes in subsurface weathering of hydrothermal sediments: a combined geochemical and microbiological investigation., Geochim. Cosmochim. Acta (in press).

[4] S. D'Hondt, B.B. Jorgensen, D.J. Miller, A. Batzke, R. Blake, B. A. Cragg, H. Cypionka, G.R. Dickens, T. Ferdelman, K.U. Hinrichs, N.G. Holm, R. Mitterer, A. Spivack, G.Z. Wang, B. Bekins, B. Engelen, K. Ford, G. Gettemy, S.D. Rutherford, H. Sass, C.G. Skilbeck, I.W. Aiello, G. Guerin, C.H. House, F. Inagaki, P. Meister, T. Naehr, S. Niitsuma, R.J. Parkes, A. Schippers, D.C. Smith, A. Teske, J. Wiegel, C.N. Padilla, J.L.S. Acosta, Distributions of microbial activities in deep subseafloor sediments, Science 306 (2004) 2216–2221.

[5] O. Nercessian, Y. Fouquet, C. Pierre, D. Prieur, C. Jeanthon, Diversity of bacteria and archaea associated with a carbonate-rich metalliferous sediment sample from the Rainbow vent field on the Mid-Atlantic Ridge, Environ. Microbiol. 7 (2005) 698–714.

[6] R.I. Amann, W. Ludwig, K.H. Schleifer, Phylogenetic identification and in situ detection of individual microbial cells without cultivation, Microbiol. Rev. 59 (1995) 143–169.

[7] M.S. Rappe, S.J. Giovannoni, The uncultured microbial majority, Annu. Rev. Microbiol. 57 (2003) 369–394.

[8] J.C. Alt, Hydrothermal oxide and nontronite deposits on seamounts in the eastern Pacific, Mar. Geol. 81 (1988) 227–239.

[9] M. Hannington, G. Thompson, P. Rona, S. Scott, Gold and native copper in supergene sulphides from the Mid-Atlantic Ridge, Nature 333 (1988) 64–66.

[10] P. Herzig, M. Hannington, S. Scott, G. Maliotis, P. Rona, G. Thompson, Gold-rich sea-floor gossans in the Troodos Ophiolite and on the Mid-Atlantic Ridge, Econ. Geol. 86 (1991) 1747–1755.

[11] C.T.S. Little, S.E.J. Glynn, R.A. Mills, Four hundred and ninety million year record of bacteriogenic iron oxide precipitation at deep-sea hydrothermal vents, Geomicrobiol. J. 21 (2004) 415–429.

[12] D. Emerson, C. Moyer, Neutrophilic Fe-oxidising bacteria are abundant at the Loihi seamount and hydrothermal vents and play a major role in Fe oxide deposition, Appl. Environ. Microbiol. 68 (2002) 3085–3093.

[13] K.J. Edwards, T.M. McCollom, H. Konishi, P.R. Buseck, Seafloor bioalteration of sulfide minerals: results from in situ incubation studies, Geochim. Cosmochim. Acta 67 (2003) 2843–2856.

[14] K.J. Edwards, D.R. Rogers, C.O. Wirsen, T.M. McCollom, Isolation and characterization of novel phsychrophili, neutrophilic, Fe-oxidizing, chemolithoautotrophic α- and γ-*Proteobacteria* from the deep sea, Appl. Environ. Microbiol. 69 (2003) 2906–2913.

[15] D.R. Rogers, C.M. Santelli, K.J. Edwards, Geomicrobiology of deep-sea deposits: estimating community diversity from low-temperature seafloor rocks and minerals, Geobiology 1 (2003) 109–117.
[16] R. Mills, H. Elderfield, J. Thomson, A dual origin for the hydrothermal component in a metalliferous sediment core from the Mid-Atlantic Ridge, J. Geophys. Res. 98 (1993) 9671–9681.
[17] P.A. Rona, Y.A. Bogdanov, E.G. Gurvich, N.A. Rimski-Korsakov, A.M. Sagalevitch, M.D. Hannington, G. Thompson, Relict hydrothermal zones in the TAG hydrothermal field, Mid-Atlantic Ridge 26°N, 45°W, J. Geophys. Res. 98 (1993) 9715–9730.
[18] M. Tivey, P. Rona, M. Kleinrock, Reduced crustal magnetization beneath relict hydrothermal mounds: TAG hydrothermal field, Mid-Atlantic Ridge, 26°N, Geophys. Res. Lett. 23 (1996) 3511–3514.
[19] P.A. Rona, S. Petersen, K. Becker, R.P.H. von Herzen, D. Mark, P.M. Herzig, J. Naka, C. Lalou, G. Thompson, Heatflow and mineralogy of TAG relict high temperature zones; Mid-Atlantic Ridge 26°N, 45°W, Geophys. Res. Lett. 23 (1996) 3507–3510.
[20] S. Severmann, R. Mills, M. Palmer, A. Fallick, The origin of clay minerals in active and relict hydrothermal deposits, Geochim. Cosmochim. Acta 68 (2004) 73–88.
[21] C. Lalou, J.L. Reyss, E. Brichet, P.A. Rona, G. Thompson, Hydrothermal activity on a 10^5-year scale at a slow-spreading ridge, TAG hydrothermal field, Mid-Atlantic Ridge 26°N, J. Geophys. Res. 100 (1995) 17,855–817,862.
[22] M.D. Hannington, The formation of atacamite during weathering of sulphides on the modern sea-floor, Can. Mineral. 31 (1993) 945–956.
[23] P.A. Rona, M.D. Hannington, C.V. Raman, G. Thompson, M.K. Tivey, S.E. Humphris, C. Lalou, S. Petersen, Active and relict sea-floor hydrothermal mineralisation at the TAG hydrothermal field, Mid-Atlantic-Ridge, Econ. Geol. 88 (1993) 1989–2017.
[24] S. Metz, J.H. Trefry, T.A. Nelsen, History and geochemistry of a metalliferous sediment core from the Mid-Atlantic Ridge at 26°N, Geochim. Cosmochim. Acta 52 (1988) 2369–2378.
[25] M.R. Palmer, and scientific party, The Interaction of Microbial Activity and Diagenesis in Hydrothermal Sediments at the Mid-Atlantic Ridge at 26°N, University of Bristol, Department of Geology, Bristol, 1996.
[26] B.W. Robinson, M. Kusakabe, Quantitative preparation of sulfur dioxide for 34S/32S analyses from sulphides by combustion with cupruous oxide, Anal. Chem. 47 (1975) 1179–1181.
[27] M.L. Coleman, M.P. Moore, Direct reduction of sulfates to sulfur dioxide for isotopic analysis, Anal. Chem. 50 (1978) 1594–1595.
[28] S. Shearme, D.S. Cronan, P.A. Rona, Geochemistry of sediments from the TAG hydrothermal field, MAR at latitude 26°N, Mar. Geol. 51 (1983) 269–291.
[29] H.C. Goulding, R.A. Mills, R.W. Nesbitt, Precipitation of hydrothermal sediments on the active TAG mound: implications for ochre formation, in: R.A. Mills, K. Harrison (Eds.), Modern Ocean Floor Processes and the Geological Record, Special Publication-Geological Society of London, vol. 148, 1998, pp. 201–216.
[30] M.R. Scott, R.B. Scott, J.W. Morse, P.R. Betzer, L.W. Butler, P. A. Rona, Metal-enriched sediments from the TAG hydrothermal field, Nature 276 (1978) 811–813.
[31] R.A. Mills, D.M. Wells, S. Roberts, Genesis of ferromanganese crusts from the TAG hydrothermal field, Chem. Geol. 176 (2001) 283–293.
[32] R. Zierenberg, W.C. Shanks, Mineraology and geochemistry of epigenetic features in metalliferous sediments, Atlantic II Deep, Econ. Geol. 78 (1983) 57–72.
[33] K.E. Peters, C.C. Walters, J.M. Moldowan, The Biomarker Guide, Cambridge University Press, Cambridge, UK, 2005, 1155 pp.
[34] M. Hannington, The formation of atacamite during weathering of sulphides on the modern seafloor, Can. Mineral. 31 (1993) 945–956.
[35] M. Thornber, Supergene alteration of sulphides: VII. Distribution of elements during the gossan-forming process, Chem. Geol. 53 (1985) 279–301.
[36] B. Dold, Enrichment processes in oxidizing sulfide mine tailings: reasons for supergene ore formation, Soc. Geol. Newsl. 16 (2003) 1–15.
[37] G. Constantinou, G. Govett, Geology, geochemistry, and genesis of Cyprus sulfide deposits, Econ. Geol. 68 (1973) 843–858.
[38] B. Dold, L. Fontbote, A mineralogical and geochemical study of element mobility in sulfide mine tailings of Fe-oxide Cu–Au deposits from the Punta del Cobre belt, northern Chile, Chem. Geol. 189 (2002) 135–163.
[39] M.D. Hannington, G.E.M. Hall, J. Vaive, Acid pore fluids from an oxidizing sulfide deposit on the Mid-Atlantic Ridge—implications for supergene enrichment of gold on the seafloor, Abstr. Programs-Geol. Soc. Am. 22 (3) (1990) 42.
[40] M.D. Hannington, P.M. Herzig, G. Thompson, P.A. Rona, Metalliferous sulfide-oxide sediments from the TAG hydrothermal field (26°N), Mid-Atlantic Ridge, EOS Trans. AGU 71 (1990) 1653 (Fall Meet. Suppl.).
[41] C. Kennedy, S. Scott, F. Ferris, Characterization of bacteriogenic iron oxide deposits from Axial Volcano, Juan de Fuca Ridge, Northeast Pacific Ocean, Geomicrobiol. J. 20 (2003) 199–214.
[42] C. Kennedy, R. Martinez, S. Scott, F. Ferris, Surface chemistry and reactivity of bacteriogenic iron oxides from Axial Volcano, Juan de Fuca Ridge, Northeast Pacific Ocean, Geomicrobiology 1 (2003) 59–69.
[43] C. Kennedy, S. Scott, F. Ferris, Ultrastructure and potential subseafloor evidence of bacterigenic iron oxides from Axial Volcano, Juan de Fuca Ridge, Northeast Pacific Ocean, FEMS Micobiol. Ecol. 43 (2003) 247–254.
[44] D. Emerson, N. Revsbech, Investigation of an iron-oxidising microbial mat community located near Aarhus, Denmark: field studies, Appl. Environ. Microbiol. 60 (1994) 4022–4031.
[45] M. Heldal, O. Tumyr, Gallionella from metalimnion in an eutrophic lake: morphology and X-ray energy dispersive microanalysis of the apical cells and stalks, Can. J. Microbiol. 29 (1983) 303–308.
[46] W.C. Ghiorse, Biology of iron- and manganese depositing bacteria, Annu. Rev. Microbiol. 38 (1984) 515–550.
[47] M. Halbach, P. Halbach, V. Luders, Sulfide-impregnated and pure silica precipitates of hydrothermal origin from the Central Indian Ocean, Chem. Geol. 182 (2002) 357–375.
[48] S.K. Juniper, Y. Fouquet, Filamentous iron–silica deposits from modern and ancient hydrothermal sites, Can. Mineral. 26 (1988) 859–869.
[49] L. Hopkinson, S. Roberts, R. Herrington, J. Wilkinson, Self-organization of submarine hydrothermal siliceous deposits: evidence from the TAG hydrothermal mound, 26°N Mid-Atlantic Ridge, Geology 26 (1998) 347–350.
[50] B.R.T. Simoneit, A.Y. Lein, V.I. Peresypkin, G.A. Osipov, Composition and origin of hydrothermal petroleum and associated lipids in the sulfide deposits of the Rainbow field (Mid-

Atlantic Ridge at 36°N), Geochim. Cosmochim. Acta 68 (2004) 2275–2294.
[51] D. Brincat, G. Abbott, Some aspects of molecular biogeochemistry of laminated and massive rocks from the Naples Beach Section (Santa Barbara–Ventura Basin), in: C.M. Isaacs, J. Rullkotter (Eds.), The Monterey Formation: From Rocks to Molecules, Columbia University Press, 2001, pp. 140–149.
[52] F. Kenig, D.-J.H. Simons, D. Crich, J.P. Cowen, G.T. Ventura, T. Rehbein-Khalily, Structure and distribution of branched aliphatic alkanes with quaternary carbon atoms in Cenomanian and Turonian black shales of Pasquia Hills (Saskatchewan, Canada), Org. Geochem. 36 (2005) 117–138.
[53] H. Chiba, N. Uchiyama, D.A.H. Teagle, Stable isotope study of anhydrite and sulphide minerals at the TAG hydrothermal mound, Mid-Atlantic Ridge, 26°N, in: P.M. Herzig, S.E. Humphris, D.J. Miller, R.A. Zierenberg (Eds.), Proc. ODP, Sci. Results, vol. 158, Ocean Drilling Program, College Station, TX, 1998, pp. 85–90.
[54] J.B. Gemmell, R. Sharpe, Detailed sulphur-isotope investigation of the TAG hydrothermal mound and stockwork zone, 26°N, Mid-Atlantic Ridge, in: P.M. Herzig, S.E. Humphris, D.J. Miller, R.A. Zierenberg (Eds.), Proc. ODP, Sci. Results, vol. 158, Ocean Drilling Program, College Station, TX, 1998, pp. 71–84.
[55] P.M. Herzig, S. Petersen, M.D. Hannington, Geochemistry and sulfur-isotopic composition of the TAG hydrothermal mound, Mid-Atlantic Ridge, 26°N, in: P.M. Herzig, S.E. Humphris, D. J. Miller, R.A. Zierenberg (Eds.), Proc. ODP, Sci. Results, vol. 158, Ocean Drilling Program, College Station, TX, 1998, pp. 47–70.
[56] R. Knott, Y. Fouquet, J. Honnorez, S. Petersen, M. Bohn, Petrology of hydrothermal mineralization: a vertical section through the TAG mound, in: P.M. Herzig, S.E. Humphris, D.J. Miller, R.A. Zierenberg (Eds.), Proc. ODP, Sci. Results, vol. 158, Ocean Drilling Program, College Station, TX, 1998, pp. 5–26.
[57] W. Shanks, Stable isotopes in seafloor hydrothermal systems: vent fluids, hydrothermal deposits, hydrothermal alteration, and microbial processes, Rev. Mineral. Geochem. 43 (2001) 470–525.
[58] J. Thompson, F. Ferris, Cyanobacterial precipitation of gypsum, calcite and magnesite from natural alkaline lake water, Geology 18 (1990) 995–998.
[59] S. Schultze-Lam, G. Harauz, T. Beveridge, Participtation of a cyanobacterial S-layer in fine grain mineral formation, J. Bacteriol. 174 (1992) 7971–7981.
[60] L.A. Warren, F.G. Ferris, Continuum between sorption and precipitation of Fe(III) on microbial surfaces, Environ. Sci. Technol. 32 (1998) 2331–2337.
[61] H.G. Thode, J. Monster, Sulfur isotope geochemistry of petroleum, evaporites and ancient seas, Mem. - Am. Assoc. Pet. Geol. 4 (1965) 367–377.
[62] L. Toran, R.F. Harris, Interpretation of sulfur and oxygen isotopes in biological and abiological sulfide oxidation, Geochim. Cosmochim. Acta 53 (1989) 2341–2348.
[63] R.O. Rye, P.M. Bethke, M.D. Wasserman, The stable isotope geochemistry of acid sulfate alteration, Econ. Geol. 87 (1992) 225–262.
[64] S. Roberts, W. Bach, R.A. Binns, D.A. Vanko, Y.C.J. D.A.H. Teagle, K. Blacklock, J.S. Blusztajn, A.J. Boyce, M. Cooper, N. Holland, B. McDonald, Contrasting evolution of hydrothermal fluids in the PACMANUS system, Manus Basin: the Sr and S isotope evidence, Geology 31 (2003) 805–808.
[65] D.K. Nordstrom, Aqueous pyrite oxidation and the consequent formation of secondary minerals, in: J.A. Kittrick, D.S. Fanning, I.R. Hossner (Eds.), Acid Sulphate Weathering: Pedogeochemistry and Relationship to Manipulation of Soil Materials, Soil. Sci. Soc. Am. Press, Madison, WI, 1982, pp. 37–56.
[66] D. Emerson, C. Moyer, Isolation and characterisation of novel iron-oxidising bacteria that grow at circumneutral pH, Appl. Environ. Microbiol. 63 (1997) 4784–4792.
[67] C.M. Bethke, Geochemical Reaction Modelling, Oxford University Press, 1996, 397 pp.